Structure and diffusion pathways in Li_6PS_5Cl argyrodite from neutron diffraction, pair-distribution function analysis and NMR

Ruth Schlenker[*,†], Anna-Lena Hansen[*], Anatoliy Senyshyn[‡], Tatiana Zinkevich[⁊], Michael Knapp[*], Thomas Hupfer[†], Helmut Ehrenberg[*], Sylvio Indris[*]

** Institute for Applied Materials (IAM), Karlsruhe Institute of Technology (KIT), Hermann-von-Helmholtz-Platz 1, 76344 Eggenstein-Leopoldshafen, Germany*

† Robert Bosch GmbH, Corporate Sector Research and Advance Engineering, Robert-Bosch-Campus 1, D-71272 Renningen, Germany

‡ Heinz Maier-Leibniz Zentrum (MLZ), Technische Universität München, Lichtenbergstr. 1, 85748 Garching, Germany

⁊ Helmholtz-Institute Ulm for Electrochemical Energy Storage (HIU), P.O. Box 3640, 76021 Karlsruhe, Germany

KEYWORDS: Li ion pathway, neutron powder diffraction, local structure, pair distribution function, Li ion hopping mechanism

ABSTRACT: The interest in all solid-state batteries has increased notably over the last years. Reasons are, among others, the demand for higher energy densities in storage devices and considerable safety issues in classical battery systems based on liquid electrolytes. One solution is the usage of solid electrolytes in battery systems. Because the crystal structure highly correlates with ion migration, the focus of our work is a detailed determination of the structure and Li pathways in the solid electrolyte argyrodite-type Li_6PS_5Cl. With neutron diffraction an additional Li site was experimentally detected. The comparison of maximum entropy method and differential bond valence analysis revealed the Li ion hopping pathways. With pair-distribution function analysis, a distortion of the $[PS_4]^{3-}$ tetrahedra resulting in a local monoclinic structure is found. A modulation of the local monoclinic structure is averaged out on longer length scales to an overall cubic structure that is known from literature.

INTRODUCTION

Energy storage is one of the major global challenges and it becomes more important as the demand for energy consuming devices is growing. [1,2] Batteries are most commonly used in a variety of portable applications, e.g. smart phones and laptops, and also in electronic vehicles. Nowadays typical batteries commonly use liquid electrolytes, but these types of electrolytes have safety concerns such as leakages and flammability. [3–5] An alternative to minimize this danger are all solid-state batteries (ASSB) based on solid electrolytes (SE) which started to be intensively investigated in the last couple of years. [6] In addition, higher volumetric and specific energy densities can be achieved by replacing liquid electrolytes by SE in combination with Li metal anodes. [7] Different material classes are discussed as SE such as polymers, oxides, phosphates and thiophosphates. [5,8–11] Conductivities up to 10^{-3} S/cm at around 80 °C were determined in polymers (PEO: Li salts) [8] whereas some oxides show a Li ion conductivity in the range of 10^{-3} S/cm at room temperature. [12,13] Inorganic solid electrolytes with oxide frameworks such as NASICON (sodium super ionic conductor) or garnet offer good chemical stabilities, but they suffer from large grain boundary resistances. [10,14,15] Sulfide-based SEs exhibit a high ionic conductivity at room temperature up to 10^{-2} S/cm. [15–17] Li thiophosphates with an argyrodite type structure (e.g. Li_6PS_5Cl) are included as a part of the sulfidic SEs and Deiseroth *et al.* [18] reported very high conductivities up to 10^{-2} S/cm which is in the range of liquid electrolytes.[19]

Ion migration is related to structural properties such as occupational defects and distortions. [18,20] Therefore, it is important to understand the role of structural peculiarities. The structural properties of argyrodites, especially Li_6PS_5X (X=Cl, Br, I), are not fully understood yet. [20–22] In the studies of Rayavarapu *et al.* [23] a NPD refinement with an additional Li site (24g) in Li_6PS_5Cl was not possible. With bond valence techniques and density-functional theory molecular dynamics approaches, the Li diffusion pathway in its structure was predicted but a sufficient experimental confirmation is still missing. [21,23–27] A pair distribution function (PDF) study reported an additional peak on a local scale but unfortunately the corresponding atom pair could not be identified. [22] This work sheds more light on the structural properties of Li_6PS_5Cl. One approach is to use the analysis of differential Fourier maps illustrating residual nuclear density used for localization of atoms and overall check of the model. This together with the nuclear densities obtained using maximum entropy analysis of structure factors yielded were used for the determination of Li ion hopping pathway. For the Li pathways, a differential bond valence approach will be compared to a maximum entropy method (MEM). The Fourier maps are based on experimental neutron diffraction data at both room temperature and elevated temperatures are taken into account. Furthermore, to investigate the structure on a local scale X-ray total scattering experiments were performed to obtain the corresponding PDF. In addition, ^{6}Li and ^{31}P magic-angle spinning (MAS) nuclear magnetic resonance (NMR) spectroscopy gives insights into the atomic environment around these elements. Temperature-dependent ^{7}Li NMR measurements including line shape analysis, relaxation time measurements, and field-gradient

NMR, are used to investigate the Li ion dynamics on different time and length scales.

EXPERIMENTAL

Li_6PS_5Cl powder (< 99 %) was purchased from NEI Corporation company. Elastic coherent neutron scattering was performed at the high-resolution neutron powder diffractometer SPODI at the neutron research reactor FRM II (Garching, Germany) [28] at a wavelength of 1.54832 Å. Powder samples were filled into niobium tubes (ca. 60 mm in height, 10 mm in diameter, 0.5 mm wall thickness) under argon and sealed using arc welding. The sample container was mounted into a high-temperature vacuum furnace. Measurements were performed in Debye-Scherrer geometry. Data collection was carried out at ambient temperature and at 500 °C. Obtained 2D diffraction patterns were corrected for geometrical aberrations and 1D diffraction data were obtained via integration along the Debye-Scherrer rings. [28] Analysis of diffraction data was performed using full profile Rietveld method implemented in the program FullProf. [29] To model the peak profile shape, the pseudo-Voigt function was chosen. Background contribution was determined using a linear interpolation between selected data points in non-overlapping regions. The scale factor, zero angular shift, profile shape parameters, resolution (Caglioti) parameters, asymmetry and lattice parameters as well as fractional coordinates of atoms and their displacement parameters were varied during the fitting. Li, S, and Cl content were constrained to their nominal values. Positions 4*a*, 4*b*, 4*c* and 16*e* positions (see below) were assumed to be fully occupied.

X-ray total scattering data were collected at the high-resolution powder diffraction beam line at PETRA III (P02.1), DESY. Experiments were performed with a beam energy of 60 keV (λ = 0.20714 Å). Exact sample detector distance and detector properties were refined based on a LaB_6 (NIST 660b) measurement using the program DAWN Science. [30] The integration of 2D Data was performed using the same program. To obtain the corresponding PDF the software PDFgetX3 was used (Q_{max} = 19 Å^{-1}). The instrumental contribution to the PDF was determined using a Ni reference measurement (Q_{damp} = 0.0215).

^6Li and ^{31}P MAS NMR measurements were performed at a magnetic field of 11.4 T corresponding to resonance frequencies of 73.6 and 202.5 MHz, respectively. Spinning was performed at 30 kHz with 2.5 mm zirconia rotors. Spectra were acquired with a Hahn-echo pulse sequence and a recycle delay of 60 s. The $\pi/2$ pulse length was 2.7 μs for ^6Li and 2.95 μs for ^{31}P. The chemical shifts were referenced to an aqueous 1M ^6LiCl solution (^6Li) and H_3PO_4 (85 %, ^{31}P). Temperature-dependent static ^7Li NMR spectra were acquired at a field of 4.7 T (77.8 MHz) with a quadrupolar-echo pulse sequence, a $\pi/2$ pulse length of 3-3.5 μs, and a pulse spacing of 30 μs. ^7Li relaxation times T_1 and $T_{1\rho}$ were measured with a saturation-recovery and a spin-locking pulse sequence, respectively. The power of the spin-locking pulse was equivalent to a nutation frequency of 37 kHz.

^7Li pulsed field gradient (PFG) NMR measurements were performed at a magnetic field of 7.0 T (116.6 MHz) and pulsed field gradients of up to 30 T/m. A stimulated-echo pulse sequence with bipolar gradients was used to observe the echo damping as a function of gradient strength.

Electrochemical impedance data were obtained by a Gamry Reference 600 in a frequency range of 0.1 Hz to 1 MHz. 100 mg of powder are pressed into a pellet with a diameter of 10 mm at a weight load of 4.3 t (resulting thickness = 750 μm). Two blocking steel electrodes with a 10 mm diameter are used in an EL-Cell. Impedance spectra were analyzed by RelaxIS software.

RESULTS AND DISCUSSION

Neutron diffraction was used to investigate the Li^+ ion distribution in the crystal structure of Li_6PS_5Cl. The initial model for the crystal structure was taken from Deiseroth et al.. [18] At room temperature, Li_6PS_5Cl has a cubic crystal structure that corresponds to the non-centrosymmetric space group F-43m (No. 216). Li and P occupy 48*h* and 4*b* Wyckoff sites, respectively. In unsubstituted argyrodites Li_7PS_6, S is placed on 4*a*, 4*c* and 16*e* Wyckoff sites. [31] In Cl containing argyrodites the Cl substitutes either 4a sites completely or partially 4*a* and 4*d* sites. [18,22]

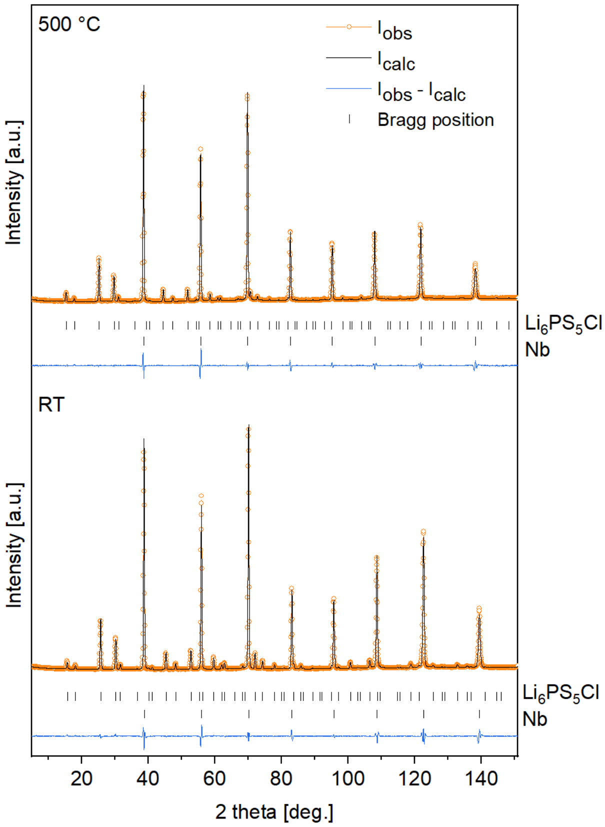

Fig. 1: Results of Rietveld refinement for neutron powder diffraction data at room temperature (bottom) and at 500 °C (top). Calculated positions of Bragg reflections are shown by vertical tick marks. The bottom row of tick marks corresponds to reflections of the Nb sample container. No phase transition is observed.

The neutron diffraction pattern measured at room temperature is shown in Fig. 1 and the structural parameters are given in Tab. 1. As the sample was placed in a Nb container, reflections of Li_6PS_5Cl and Nb can be identified which are included in the refinement and marked in Fig. 1. The analysis of the differential Fourier map shows a minimum on the nuclear density map at the 48h Wyckoff site (0.047(3), 0.253(9), ½ + 0.047(3) which represents a new Li site. The negative nuclear density indicates a preferable lithium (Li2) occupation of this 48h site. Its occupancy was refined to 0.09(2) %. Results of high temperature neutron powder diffraction are consistent with the room temperature diffraction pattern. Heating the sample to 500 °C (before decomposition) did not reveal any phase transition (Fig. 1b).

.

Tab. 1: Experimental structural parameters of Li_6PS_5Cl at ambient temperature and *T* = 500 °C (orange color). The space group is F-43m (No. 216). Numbers in parentheses give statistical deviations in the last significant digit. Obtained lattice parameter at ambient temperature and *T* = 500 °C were 9.8482(2) Å and 10.0186(3) Å, respectively. Restraints are set according to the chemical composition Li_6PS_5Cl (site occupation: Li1 + Li2 = 0.5, P = S1 =S2/Cl2 = S3/Cl3 = 1.0).

Atom site	Wyckoff	*x/a*, frac.un.	*y/b*, frac.un.	*z/c*, frac.un.	B_{iso}, Å^2	SOF, frac.un.
Li1	48*h*	0.3229(15)	0.0257(13)	0.6771(15)	4.0*	0.41(1)
		0.345(2)	*0.031(3)*	*0.655(2)*	*12.5**	*0.41(3)*
Li2	48*h*	0.047(4)	0.254(9)	0.547(4)	2.3(9)	0.09(1)
		0.047(3)	*0.253(9)*	*0.547(3)*	*1.2(9)*	*0.09(3)*
P	4*b*	½	½	½	2.4(1)	1.0
					4.9(4)	
S1	16*e*	0.1206(7)	-0.1206(7)	0.6206(7)	3.2(1)	1.0
		0.1157(11)	*-0.1157(11)*	*0.6157(11)*	*6.6(3)*	
S2/Cl2	4*a*	0	0	0	2.7(2)	0.538(6)/0.462(6)
					6.8(4)	*0.54(1)/0.46(1)*
S3/Cl3	4*d*	¾	¾	¾	2.6(1)	0.462(6)/0.538(6)
					4.7(2)	*0.46(1)/0.54(1)*

Fit residuals: R_p = 3.85 %; R_{wp} = 5.76 %; R_{exp} = 1.54 %, Chi2: 14.0

R_p = 3.42 %; R_{wp} = 5.23 %; R_{exp} = 1.53 %, Chi2: 11.7

* for the Li1 site the displacement parameters were simulated in anisotropic approximation. At ambient temperatures components of anisotropic displacement parameters for Li1 site were following (u_{11}, u_{22}, u_{33}, u_{12}, u_{13}, u_{23}): 0.065(7), 0.022(9), 0.065(7), 0.002(5), 0.002(9), and -0.002(5) Å^2. At 500 °C: 0.22(5), 0.04(2), 0.22(5), 0.024(11), 0.07(5), and -0.024(11) Å^2.

The theoretical Li distribution in Li_6PS_5Cl was estimated using differential bond valences [32] on the basis of atomic positions of P and S/Cl atoms in the crystal structure. The obtained differential bond valence maps (marked in yellow and green in Fig. 2) are consistent with molecular dynamic simulations reported by Yu et al.. [27] The figure shows a triangular arrangement of Li1 atoms. Between these Li1 atoms, the newly found Li2 atoms are observed. Rao et al. [24,25] described interstitial sites between Li1 sites forming a hexagon in their bond valence calculations. Rayavarapu et al. [23] used a model with only Li1 sites but mentioned a possible additional Li2 site. Four of those hexagons form a tetrahedral Li cage which is placed around S and Cl. The interconnections of the cages are marked in yellow. The cages are connected to each other via Li1-Li1 and Li1-Li2 bridges marked in grey. As described by Yu et al. [27] three different Li transitions are identified: exchange within the cage segment, intra-cage and inter-cage transitions. The Li2 atomic site determined by Fourier analysis of differential nuclear densities proves to be part of the cage structure formed by Li atoms. It also indicates high Li disorder and the involvement of both Li1-Li2 into the Li exchange within one cage segment. The differential bond-valence approach predicts Li pathways defined by the atomic positions and orientation of coordination polyhedra. Two possible pathways that interconnect Li cages (i.e. these correspond to 3D Li diffusion in Li_6PS_5Cl) are predicted: Li diffusion via long Li1-Li1 bridges through the neck at 16*e* (0.365, 0.365, 0.135) and a short pathway of Li2-Li2 via 24*f* site (0.285, ½, 0).

The PS_4 tetrahedra in Li_6PS_5Cl are formed by four equal P-S/Cl distances, $d_{P-S/Cl}$=2.057(7) Å. The local Li arrangement is highly disordered forming a number of short Li - Li site distances: $d_{Li1-Li2}$=1.46(4) Å defines the Li cage segment; the distances $d_{Li1-Li1}$=2.03(2) Å and $d_{Li1-Li1}$=2.11(2) Å might be related to the transport within the tetrahedral Li cage, while the short $d_{Li2-Li2}$=1.31(5) Å is attributed to inter-cage Li diffusion. Furthermore, the Li cations are also tetrahedrally surrounded by S/Cl, where four Li-S/Cl distances occur: for Li1 – $d_{Li1-S3/Cl3}$=2.431(1) Å, $d_{Li1-S2/Cl2}$=2.480(1) Å and two distances of type d_{Li1-S1}=2.521(2) Å; for Li2 – two d_{Li2-S1}=2.521(2) Å distances, $d_{Li2-S2/Cl2}$=2.51(9) Å, $d_{Li2-S3/Cl3}$=2.83(4) Å. A high degree of Li disorder can be concluded by the analysis of obtained displacement parameters, where the Li1 site displays significantly higher disorder in comparison to Li2. High degree of Li disorder even at low temperatures is a characteristic feature for superionic Li conductors. [33]

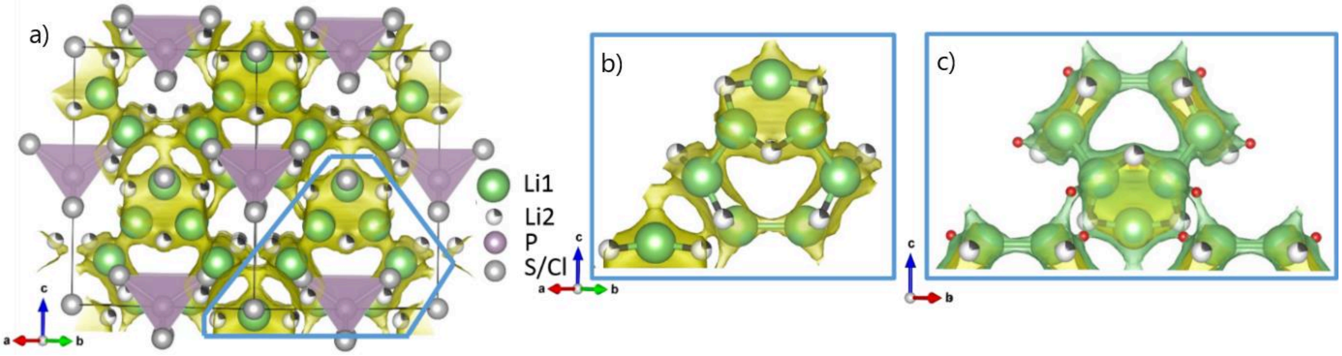

Fig. 2: a) Bond valence isosurfaces and atom locations in Li_6PS_5Cl. The $[PS_4]^{3-}$ tetrahedra are coloured in purple and the yellow/green isosurfaces correspond to b) ΔV=0.12 and c) ΔV=0.1 val. un., accordingly. Red spheres illustrate necks/intermediate sites potentially supporting Li diffusion.

The electron and nuclear density maps give information about the Li diffusion pathways in the structure. However, the direct derivation from the powder diffraction data is often limited. The Fourier analysis mentioned before can be used for the localization of atomic species but the determination of diffusion pathways is also limited due to various artefacts caused by limited statistics in powder diffraction measurements. An alternative is the maximum-entropy method (MEM). It is based on the estimation of 3D scattering densities from a limited amount of information by maximizing information entropy under restraints. This is consistent with experimentally obtained structure factors.

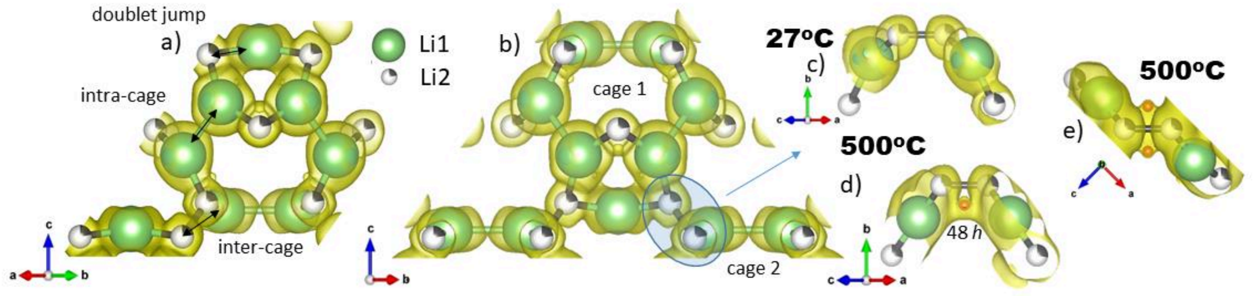

Fig. 3: Selected region of negative nuclear scattering density maps observed for Li_6PS_5Cl at ambient temperature (a-c) and 500 °C (d-e) by MEM analysis. Isosurfaces were plotted using the equidensity level 0.013 fm/Å^3 and data visualization has been performed using program VESTA. [34]

In Li_6PS_5Cl, only Li has an isotope-averaged negative scattering length (b_{Li} = -1.9 fm). Therefore, the analysis of negative nuclear density maps is used for the derivation of Li diffusion pathways. The MEM reconstruction of negative nuclear scattering density was performed by using the program Dysnomia. [35] The obtained 3D volume plot of nuclear scattering densities is pictured in Fig. 3. A threshold in the data visualization, above where no artefacts are present, was defined at around 0.013 fm/Å^3. The Li hexagonal units are clearly visible. The connection within one tetragonal Li cage (intra-cage) is indicated via Li1-Li1 bridges (Fig. 3a). However, the details on 3D Li inter-cage conductivity still require more consideration. The pathway along Li1-Li1 bridges can be excluded because of the absence of negative nuclear density in this region. However, the pathway along Li2-Li2 does not show any close connection of nuclear densities (Fig. 3c), as seen in differential bond valence approach, at the chosen threshold for the room temperature measurement.

A data collection at elevated temperatures of 500 °C gives more insight into the Li ion conduction pathway. The high temperature data are more informative due to high temperature activation of conductivity and increased Li hoping. The Li becomes less localized so that one can follow the tiny details of diffusion pathway not fully populated at ambient temperature. A complex pathway including $48h$ (0.155, 0.527, 0.345) site is found which is marked as red sphere in Fig. 3d and e. Li can diffuse directly from both Li1 and Li2 sites via the $48h$ site. This is in contrast to the differential bond valence approach which suggests the diffusion from Li2 to Li2 only via $24f$ (0.285, ½, 0) site. The observed inconsistency is not unusual. The bond-valence is approach is often considered to be a first method for prediction of ionic (either cation or anion) diffusion – right after simple consideration of crystal chemistry and/or Hirschfeld (void) analysis. The advantage of the method is that the positions of mobile species are not needed for the generation of 3D valence pathways where bond-valence corresponds to the valence of mobile ions. The method describes all possible diffusion pathways without any hint for its energetics. This may result in selected pathways having a high activation barrier in the structure that are not energetically allowed/preferable.

In summary, the three-dimensional Li diffusion pathways in Cl doped Li argyrodite type Li_6PS_5Cl were observed in neutron diffraction measurements. Differential Fourier maps, bond-valence approach and maximum-entropy method were used to identify the exact Li ion diffusion mechanism. The Li diffusion occurs in three different possible pathways: exchange within the cage segment, intra-cage and inter-cage transitions. Within the cage segment Li moves in the hexagonal Li units composed of closely connected Li1 and Li2 sites. Four of those hexagonal units form a tetragonal Li cage in which the Li moves via Li1-Li1 bridges. The distribution of negative nuclear densities reveals an enhanced Li exchange within the disordered hexagonal units whereas both intra- and inter-cage Li diffusion is limited. In order to quantify these barriers, the activation energy at each pathway was estimated with the relationship between the probability of atom location and single particle potential energy (similar to those reported in Refs. [36–38]). To ensure a valid system for classical approximation, the 500 °C dataset was used. The activation energies for diffusion within the trigonal units (Li1-Li2), intra-cage (Li1-Li1) and inter-cage (Li1-$48h$-Li1) diffusion are given in Tab. 2. These estimations of activation energies will be compared to the activation energies found in NMR and electrochemical impedance spectroscopy.

Tab. 2: Summary of the activation energies of different Li jumps in the Li_6PS_5Cl structure derived from MEM analysis.

	Doublet	Intra-cage	Inter-cage
Activation energy [eV]	0.21	0.42	0.40

As ion migration is highly correlated with structural properties, e.g. occupational defects and local distortions, a detailed structure analysis is crucial. [18,20] A review of the effect of lattice distortions and ion migration barriers revealed a discrepancy between proposed mechanisms for argyrodites and other solid state electrolytes, which indicates that the defect structure is not understood in detail. [20,22] A reported X-ray PDF study of Li_6PS_5X (X= Cl, Br, I) revealed an additional peak around 3.3 Å but unfortunately the corresponding atom pair was not addressed. [22] Our PDF of Li_6PS_5Cl revealed similar observations (Fig. 4). The above described cubic model was used to fit the structural data. Above 5 Å the modelled PDF matched the data reasonably well, but below 5 Å the discrepancy between the model and the experimental PDF becomes obvious. The strongly increased peak (not additional) at ~3.35 Å corresponds to $(S\text{-}S)_{tet}$ distances within the tetrahedra in the cubic structural model. Whereas, at ~ 3.63 Å a peak is missing in the fit which corresponds to the inter tetrahedral S_{tet}-S_{tet} distance. Using a tetragonal model (subgroup $I\bar{4}m2$, No. 119) to describe the structure gives a better agreement in the low r region but this seems to be an oversimplified model. Therefore, the low r region (< 5 Å) will be analysed in more detail.

The low r region was fitted with the tetragonal setting of the cell with a r dependent sequential fitting. While the c/a ratio is increased in the low r region, it is close to its ideal cubic value of $\sqrt{2}$ above > 15 Å. Nevertheless, the evolution of the bond angle variance, [39] which represents distortions of the $[PS_4]^{3-}$ tetrahedra, shows a higher deviation from an ideal tetrahedron with a higher r as can be seen in Fig. 5. From this r dependence it can be concluded, that the correlation length is less than 13.7 Å, which is less than three neighbouring tetrahedra. This might indicate a modulation caused by rotational disorder of neighbouring tetrahedra. If a correlated rotation of the tetrahedra is assumed, the net disorder is averaged out as long as the distance in real space does not exceed the modulation. In real-space Rietveld-approach using PDFgui, the S1 positions of the tetrahedra were refined freely and the cubic metric of the cell was fixed. The resulting overall symmetry was found to be monoclinic (space group Cm), revealing a $\sqrt{2}a$ superstructure with a modulation arrangement of the tetrahedra. A PDF pattern of low r values with the resulting monoclinic structure fit is displayed in Fig. 6. The corresponding structural comparison is shown in Fig. 7.

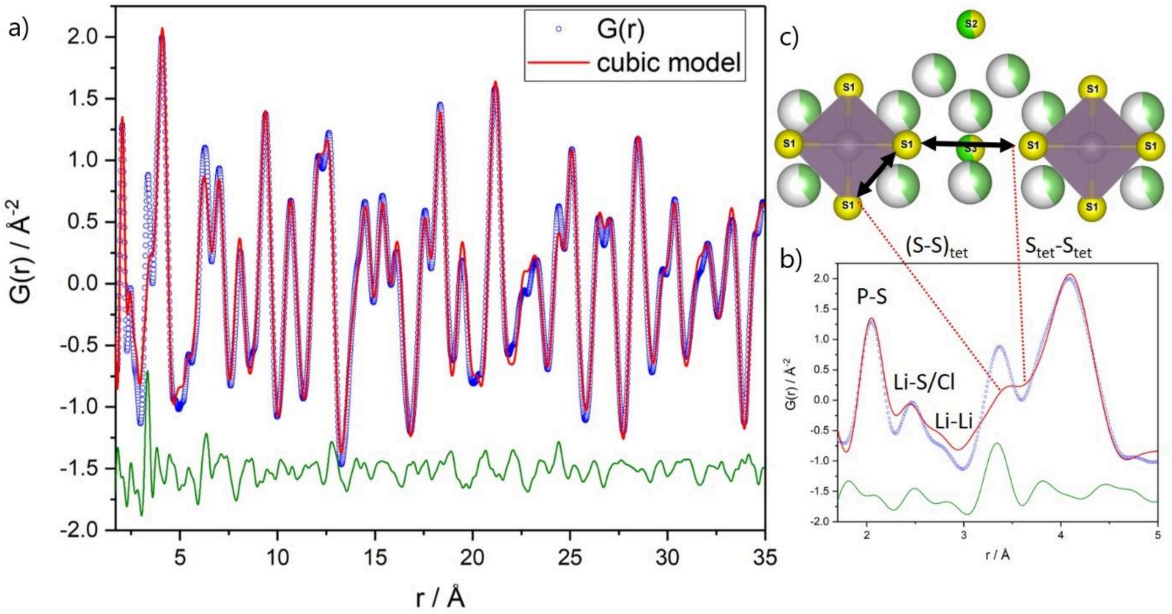

Fig. 4: PDF (blue circles) based on total scattering data collected at P02.1 at DESY. a) A PDF calculated based on a cubic argyrodite model was fitted to the observed PDF by least-square refinement. The final difference curve of the fit is depicted in green. b) A zoom into the low r region is given on the right, emphasizing the discrepancy between the model and the observed PDF. c) On the upper right a part of the structure is depicted: Li in light green, S in yellow, Cl in green, P in purple.

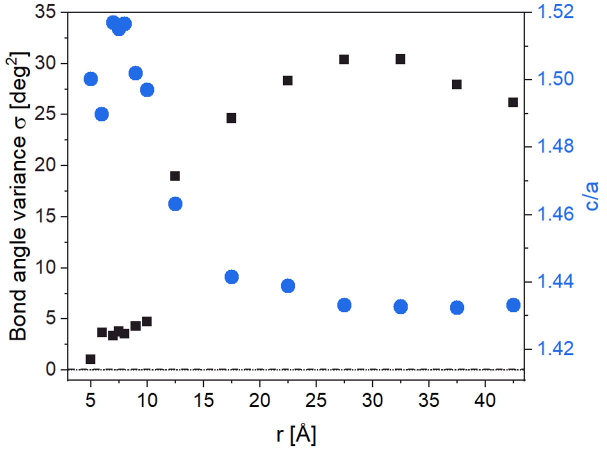

Fig. 5: Evolution of tetragonal lattice parameter c/a (blue) and bond angle variance σ (black) in dependence of r. Dotted line corresponds to ideal cubic value of 1.414 (for c/a) and 0 (for the variance), respectively. σ represents the distortion of polyhedral species, regarding their deviation from ideal bond angles.

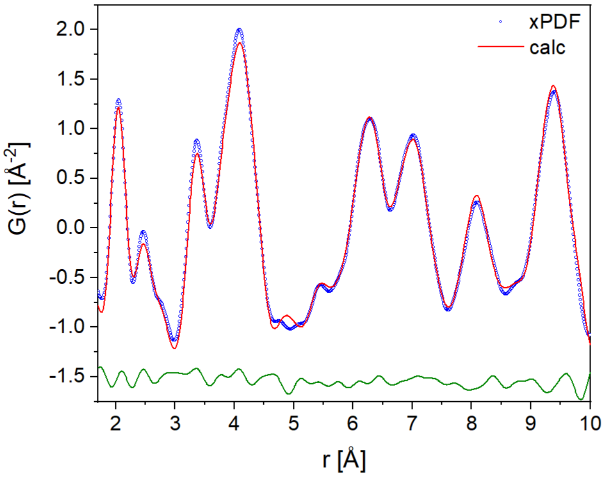

Fig. 6: PDF pattern of the low r region. The real space Rietveld approach is described in the text. In comparison to a cubic cell as shown in Fig. 7, the two peaks between 3-4 Å are fitted sufficiently well. This supports the proposed $\sqrt{2}a$ modulation that averages out over a wide r range resulting in a cubic cell structure.

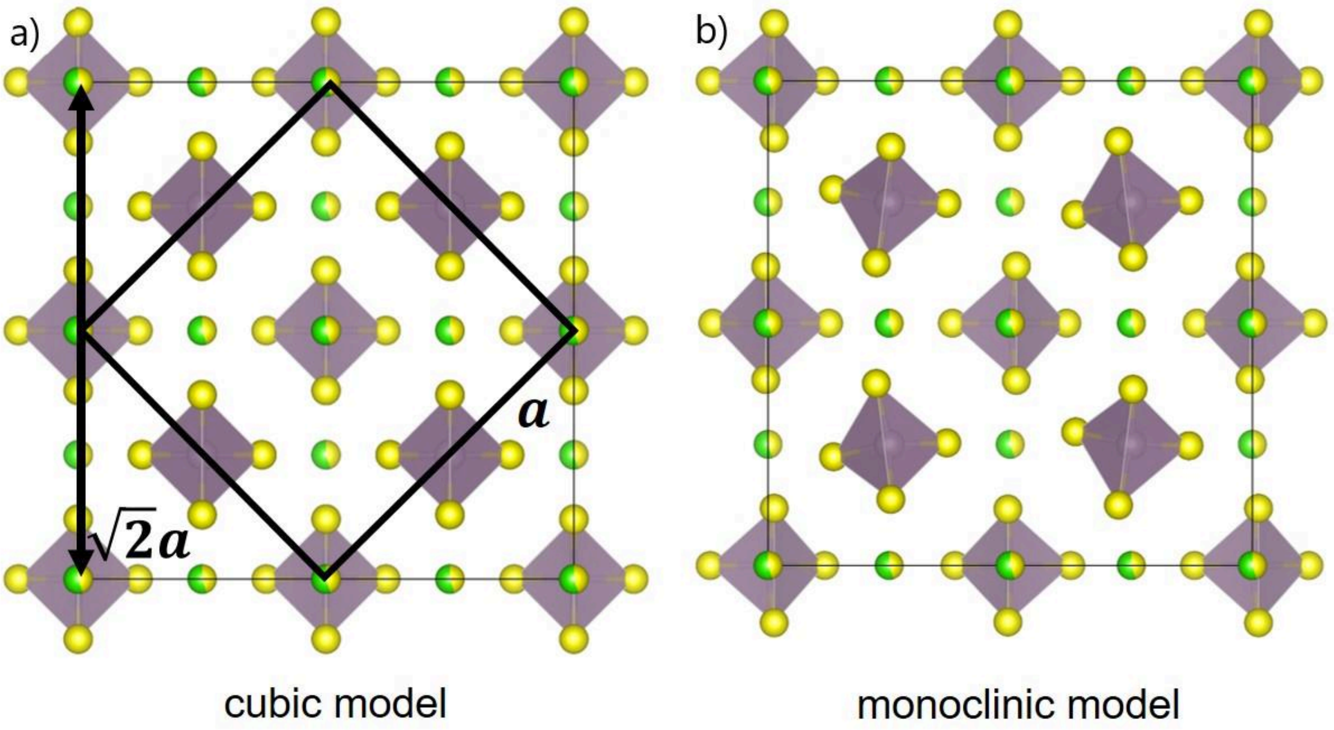

Fig. 7: Comparison of a) the cubic cell (black square) of Li_6PS_5Cl and b) our monoclinic model with a $\sqrt{2}$a modulation and rotationally disordered tetrahedra. Li ions are omitted for clarity. Cl^- are green, $[PS_4]^{3-}$ are grey with S^{2-} depicted in yellow.

^{6}Li MAS NMR measurements are used to probe the local environment around the Li ions in the Li argyrodite structure. The spectrum is illustrated in Fig. 8a. A peak in the range of 1.2 to 1.8 ppm is observed. Hanghofer *et. al* [40] showed a much narrower line shape with overlapping contributions at 1.30 ppm and 1.21 ppm. These two chemical shifts are in good agreement with our data. However, our spectrum reveals a broader line shape with contributions also at higher ppm values. This difference is attributed to larger variations in the Li environment, i.e. a higher degree of structural disorder. This might include different crystallinities, amorphous phase fractions, S/Cl anion disorder, and rotational $[PS_4]^{3-}$ disorder [40–42] which all will be influenced by the details of the synthesis procedure (synthesis temperature, quenching rate, etc.). From our previous neutron diffraction data, a new Li site Li2 and a high disorder of Li sites can be derived which might cause the broad line shape in the MAS NMR spectrum. Unfortunately, Li positions are not clearly defined in the literature [40] which makes a comparison impossible. In general, for ^{6}Li MAS NMR the contributions are better resolvable than in ^{7}Li MAS NMR where a single broad peak is observed. [18,40]

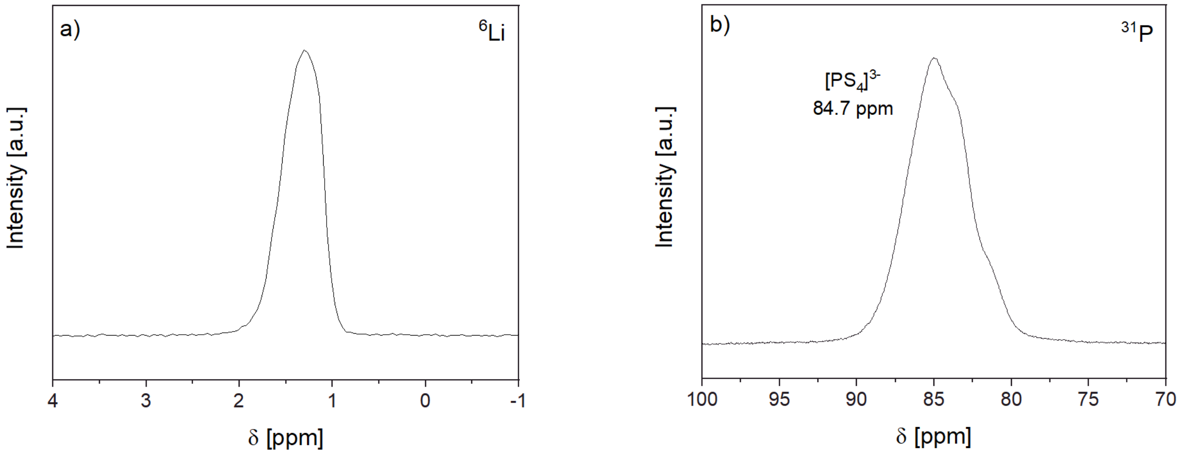

Fig. 8: a) ^{6}Li MAS NMR and b) ^{31}P MAS NMR spectra of Li_6PS_5Cl.

Fig. 8b shows the ^{31}P NMR spectrum which reveals a single broad line centered at 84.7 ppm that corresponds to isolated $[PS_4]^{3-}$ tetrahedral, with two shoulders at the right side. [37,42–46] The line shape is in good agreement with spectra described in the literature. [18,40] Its shape can be described by multiple overlapping peaks that correspond to anionic S/Cl disorder around the $[PS_4]^{3-}$ tetrahedra. [18,40] Our PDF studies discussed above reveal a symmetrical tilt of those tetrahedra (Fig. 7) which could be responsible for an additional line broadening in the ^{31}P NMR spectra.

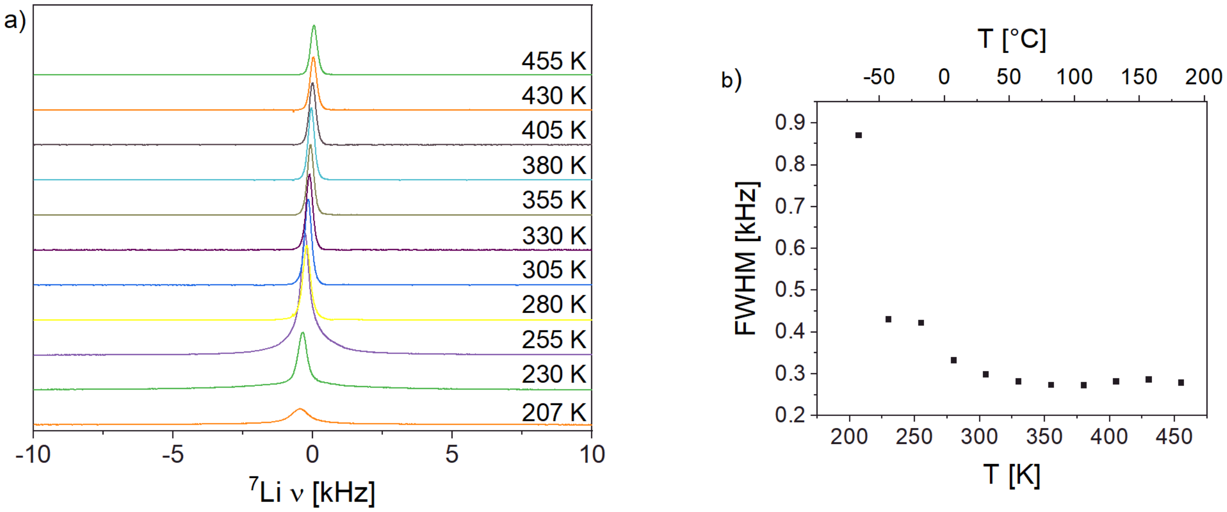

Fig. 9: Static ^{7}Li NMR spectra were acquired at different temperatures using a field of 4.7 T, corresponding to 77.8 MHz, with a quadrupolar-echo pulse sequence, a) lineshape for temperatures from 207 K to 455 K and b) line width vs temperature.

Fig. 9 presents the linewidth of the static ^{7}Li NMR spectra vs temperature for the Li_6PS_5Cl sample. It reveals a clear so-called motional narrowing, i.e. a strong decrease of the line width with increasing temperature. This happens already at temperatures well below room temperature. At low temperatures, dipolar interactions between the ^{7}Li nuclear magnetic moments cause a broad line with a width of some kHz. When the temperature is increased, the onset of fast Li hopping with motional correlation times of the order of the inverse low-temperature line width, i.e. some milliseconds, causes a temporal averaging of the local environments around the Li nuclei, resulting in a uniform resonance frequency and thus a narrow line width at elevated temperatures. At temperatures above 350 K, the residual line width of 0.25 kHz just reflects the inhomogeneity of the external magnetic field. These results are in good agreement with the literature. [27,40]

Spin-lattice relaxation times T_1 and $T_{1\rho}$ in the laboratory and in the rotating reference frame, respectively, can be used to probe local dynamics of Li ions in solids on short time scales of some ns (T_1) or µs ($T_{1\rho}$). [24,47] The relaxation of the nuclear spin system toward its equilibrium magnetization occurs via transitions between the nuclear Zeeman levels. These transitions are induced by fluctuations of the local magnetic/electric fields at the sites of the nuclei. In the simplest case, these fluctuations are described by an exponential correlation function that is characterized by the correlation time τ_c [48] which is, apart from a factor of the order of unity, equal to the average residence time τ of the Li ions between two subsequent jumps. The inverse of this average residence time is the average hopping rate τ^{-1} of the Li ions. In this case, the temperature dependence of the spin lattice relaxation rate T_1^{-1} can be described by the so-called Bloembergen-Purcell-Pound (BPP) behavior:

$$\frac{1}{T_1} \sim \frac{\tau_c}{1+(\omega_L\tau_c)^2} \qquad (1)$$

Here ω_L is the Larmor frequency of the Li nuclei. A correlated motion of the Li ions, i.e. a somehow confined fast hopping on short time/length scales corresponding to enhanced forward-backward jump probability and a slower motion on longer time/length scales, can result in deviations from this BPP behavior that can be described by

$$\frac{1}{T_1} \sim \frac{\tau_c}{1+(\omega_L\tau_c)^{1+\beta}} \qquad (2)$$

with β usually varying between 0 and 1. Similar expressions can be found for the relaxation rate $T_{1\rho}^{-1}$ in the rotating reference frame by substituting the Larmor frequency ω_L by the spin-lock frequency ω_1. [49] The temperature dependence of the hopping rate τ^{-1} can usually by described by an Arrhenius behavior

$$\tau^{-1} = \tau_0^{-1} \times \exp\left(-\frac{E_A}{k_B T}\right) \qquad (3)$$

Fig. 10 summarizes the relaxation rates as a function of inverse temperature for Li_6PS_5Cl along with the fitting according to the equations described above. The relaxation rate T_1^{-1} has a clear maximum at 311 K. From the Larmor frequency of the Li ions (2π × 77.8 MHz) an average residence time of about 2 ns can be extracted for the temperature where the maximum occurs. The slope of T_1^{-1} on the high-temperature side of this maximum reveals the energy barrier the Li ions have to overcome for the local hopping.

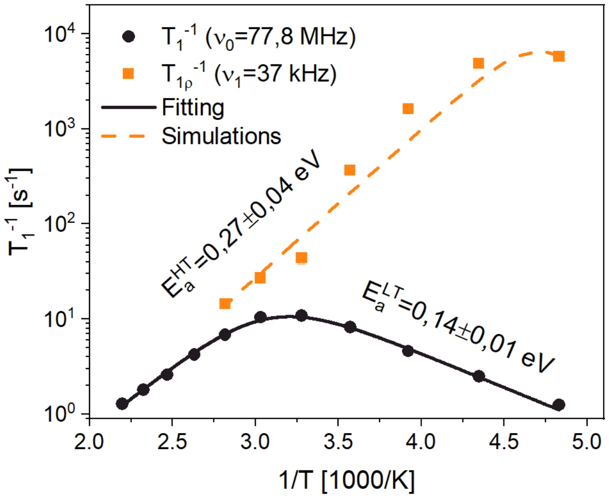

Fig. 10: ^{7}Li relaxation times T_1 and $T_{1\rho}$ were measured with a saturation-recovery and a spin-locking pulse sequence, respectively.

The Li_6PS_5Cl sample shows an asymmetric behavior with a smaller slope on the low-temperature side which is in good agreement with the literature. [27,40] This is consistent with a correlated motion of the Li ions, i.e. an enhanced forward-backward jump correlation as it can be expected for a Li hoping mediated via vacancies on the different Li sites. The lower activation energy observed on the low-temperature side (0.14 ± 0.01 eV) corresponds to local jump processes and is thus assigned to intra-cage hopping. The larger slope on the high-temperature flank (about 0.27 eV) corresponds to the long-range transport and is thus assigned to inter-cage jumps. This value is in good agreement with the activation energy determined from the $T_{1\rho}^{-1}$ data. In these experiments, due to the lower effective magnetic field, the maximum occurs at lower temperatures and therefore only the high temperature flank is observed.

With the average residence time, we can use the Einstein-Smoluchowski equation [50,51]

$$D = f \times \frac{l^2}{6\,\tau} \tag{4}$$

to get a rough estimate for the diffusion coefficient of the Li ions, here determined from the local hopping of the Li ions. We estimated the average jump length l from the shortest Li-Li inter-cage distance in the argyrodite structure (2.03 Å) and we assume that no correlations occur in the hopping of the Li ions. Using the activation energy determined from the fitting procedure we can extrapolate the diffusion coefficient to room temperature (298 K) and we obtain a value of about 2.5×10^{-12} m^2/s. From this diffusion coefficient we can use the Nernst-Einstein equation [52,53].

$$\sigma = \frac{D\, N_{\mathrm{Li}} e^2}{k_{\mathrm{B}}\, T} \tag{5}$$

to estimate the Li ion conductivity. We use the concentration of the Li ions N_{Li} (2.5×10^{28} m^{-3}), their charge e, and the Boltzmann constant k_{B}, and we assume that Li ions are moving as independent charge carriers (f = 1) to finally get an estimation of σ = 3.9 mS/cm.

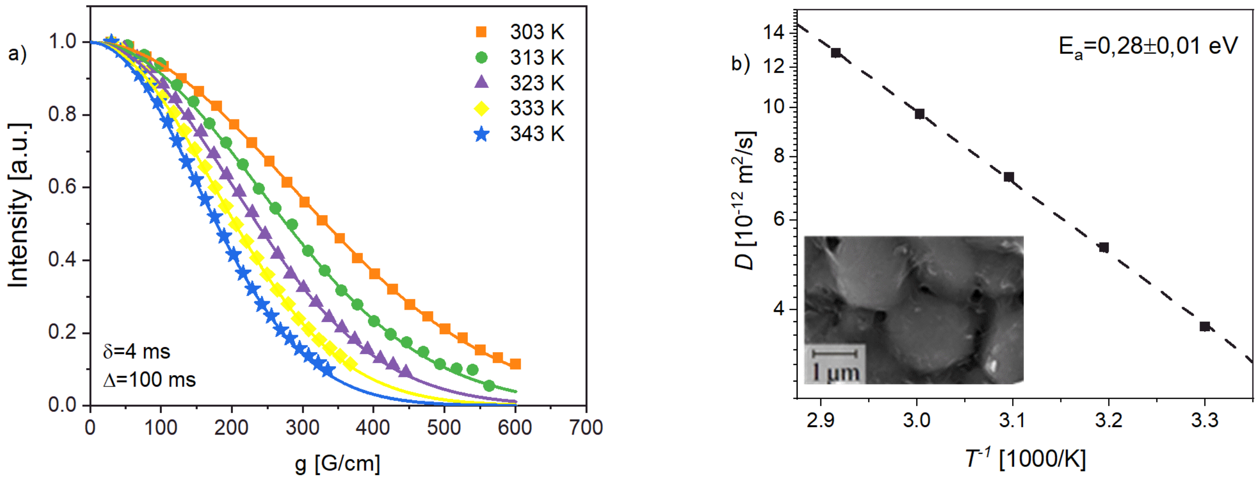

Fig. 11: a) the diffusion coefficient of the Li ions determined by PFG NMR for different temperatures, b) extracted diffusion coefficients vs. inverse temperature. The inset in b) shows SEM result of Li_6PS_5Cl sample. The average grain size is < 1.5 μm.

PFG NMR measurements can be used to investigate the long-range transport of the Li^+ ions, i.e. the motion of these ions over time scales of about one second. Fig. 11a shows the echo intensity vs gradient strength in a temperature range between 303 and 343 K. According to the Stejskal-Tanner equation [54] the echo damping can be well described with a Gaussian function.

$$I = I_0 \cdot \exp\left(-D\gamma^2 g^2 \delta^2 (\Delta - \delta/3)\right) \qquad (6)$$

Here, I_0 and I are the echo intensities without and with gradient, respectively, γ is the magnetogyric ratio, g the gradient strength, and Δ and δ are the diffusion time (0.1 s in this case) and the gradient duration (4 ms), respectively. A diffusion coefficient D can be extracted from the corresponding fit for each temperature. The diffusion coefficients in the temperature range between 303 and 343 K are shown in Fig. 11b. The temperature dependence can be well described with an Arrhenius behaviour and it reveals an activation energy of about 0.28 eV for the long-range transport of the Li ions. This value is in good agreement with that determined from the high-temperature slope of the $T_1^{-1}(T^{-1})$ data and is also in good agreement with the activation energy determined from impedance measurements (described below). It thus also confirms that the high-temperature $T_1^{-1}(T^{-1})$ data reflect the long-range transport of the Li^+ ions. The Nernst-Einstein equation [55] can be used to estimate the Li ion conductivity σ_{Li} from the Li diffusion coefficient D as described before in Eq. (4). We assume that only Li^+ ions are acting as mobile species and charge carriers. This gives a Li conductivity of about 5.1 mS/cm at room temperature. This is again in good agreement with the estimation from the relaxation time measurements and with the conductivity determined by impedance measurements. We can also estimate from the diffusion coefficient the average distance of about 1.5 µm, which the Li ions travel within the diffusion time Δ (100 ms) in this PFG NMR experiment. Considering the particle size distribution of < 1.5 µm from the SEM image in Fig. 11b, this shows that we are probing the long-range transport of Li ions inside the bulk of the grains but also across grain boundaries. The good agreement between the T_1^{-1} results, probing local hopping of the Li^+ ions, and PFG NMR results, probing the long-range transport also across grain boundaries, both in the estimated conductivities and in the activation energies, shows that the fundamental jump process observed in the T_1^{-1} measurements is also responsible for the long-range transport of the Li^+ ions. Furthermore, these results show that the grain boundaries have only a minor influence on the Li^+ ion transport in this material.

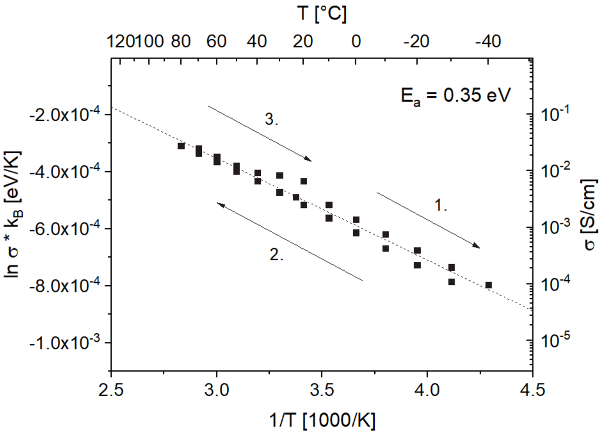

Fig. 12: Ionic conductivities derived from impedance measurements taken from -40 to 80 °C during first cooling from room temperature, followed by heating and successive cooling back to room temperature. The corresponding activation energy of 0.35 eV is in agreement with NMR measurements and literature. [24,47,56–59]

The overall conductivity of the argyrodite-type Li_6PS_5Cl was also determined by impedance spectroscopy. Fig. 12 shows the extracted dc conductivity vs inverse temperature. The dc conductivity of 3.4 mS/cm at room temperature is in very good agreement with our NMR measurements described above and also in reasonable agreement with those reported by Zhou [60] (2.4 mS/cm), Wenzel [57], Rao [24] (both 1.9 mS/cm), Yu [47] (1.2 mS/cm), and Boulineau (0.2-1.3 mS/cm). [56] Overall, the temperature dependence can be well described by an Arrhenius behavior. The activation energies are in the range of 0.32-0.37 eV which is in good agreement with literature data. [24,47,56–59] These calculated activation energies from EIS measurements are slightly higher (23 %) than the measured activation energies from our PFG NMR data (0.28 – 0.30 eV). Such deviations between EIS and NMR measurements is seen in literature as well. [37] The small difference might be attributed to the different time scales probed in impedance measurements and PFG NMR. While the dc conductivity extracted from the impedance measurements corresponds to the long-range transport, i.e. the overall effective conductivity including bulk and grain boundary contributions, PFG NMR is probing the mean square displacement of the Li ions over the diffusion time Δ (0.1 s). Therefore, with the room-temperature diffusion coefficient determined from PFG NMR we can estimate that, within the diffusion time Δ, PFG NMR is probing average displacements of about one 1 µm and thus PFG NMR might detect a weaker influence of the grain boundaries as the average particle size is about 1.5 µm.

CONCLUSION

In summary, with Fourier maps derived from neutron diffraction data, a new Li2 site was found that has an occupancy of 9 % whereas the Li1 site reported in literature has an occupancy of 41 %. Further neutron diffraction studies at elevated temperatures in combination with differential bond valence and maximum entropy methods reveal that the new Li site contributes to Li hopping pathways. A short-range hopping occurs from Li1 to Li2 sites within a Li hexagon. From one Li hexagon to another hexagon within a Li cage, the intra-cage Li pathways are formed via Li1-Li1 sites. The inter-cage Li hopping from one cage to the next one can occur from both Li1 or Li2 via a 48*h* site to another Li1 or Li2 site. The theoretical differential bond valence approach predicts two possible pathways for inter-cage hopping: Li1-Li1 via a 16*e* site and Li2-Li2 via 24*f*. This could not be confirmed by the maximum entropy method based on obtained neutron diffraction data that revealed an inter-cage pathway from Li1/Li2 – 48*h* (0.155, 0.527, 0.345) – Li1/Li2. In addition, PDF studies reveal a tilting of the $[PS_4]^{3-}$ tetrahedra that lead to a local monoclinic structure. This local monoclinic structure is modulated throughout higher *r* values which leads to a global averaging towards a cubic structure. The predicted high disorder of Li sites can be supported by NMR studies. Furthermore, the ^{6}Li and ^{31}P MAS NMR analysis supports the interpretation of a high disorder in the Li_6PS_5Cl structure. A fast Li-ion motion at ambient temperatures can be derived from the ^{7}Li NMR line shapes. The relaxation rate T_1^{-1} reveals an asymmetric behavior, which is consistent with a correlated motion caused by multiple activation barriers the Li ions have to overcome for the long-range transport in the Li_6PS_5Cl structure. A comparison with the NPD and MEM results shows that the local hopping is related to the doublet jump, whereas the long-range diffusion corresponds to the intra- and intercage hopping pathways. The Li^+ diffusion coefficient is 2.5×10^{-12} m^{2}s^{-1} and the ionic conductivity is 3.9 mScm^{-1} at 298 K which is in good agreement with the PFG NMR, EIS results and the literature. [24,47,56,57,60]

ACKNOWLEDGEMENT

We are grateful to Robert Bosch GmbH for financial support. This work contributes to the research performed at CELEST (Center for Electrochemical Energy Storage Ulm-Karlsruhe) and was partially supported from the Federal Ministry of education and Research (BMBF) within the FestBatt project (03XP0176A).

LITERATURE

(1) Scrosati, B.; Garche, J. Lithium Batteries: Status, Prospects and Future. *J. Power Sources* **2010**, *195* (9), 2419–2430. https://doi.org/10.1016/j.jpowsour.2009.11.048.

(2) Etacheri, V.; Marom, R.; Elazari, R.; Salitra, G.; Aurbach, D. Challenges in the Development of Advanced Li-Ion Batteries: A Review. *Energy Environ. Sci.* **2011**, *4* (9), 3243. https://doi.org/10.1039/c1ee01598b.

(3) Fergus, J. W. Ceramic and Polymeric Solid Electrolytes for Lithium-Ion Batteries. *J. Power Sources* **2010**, *195* (195), 4554–4569. https://doi.org/10.1016/j.jpowsour.2010.01.076.

(4) Xin, S.; You, Y.; Wang, S.; Gao, H.-C.; Yin, Y.-X.; Guo, Y.-G. Solid-State Lithium Metal Batteries Promoted by Nanotechnology: Progress and Prospects. *ACS Energy Lett.* **2017**, *2* (6), 1385–1394. https://doi.org/10.1021/acsenergylett.7b00175.

(5) Knauth, P. Inorganic Solid Li Ion Conductors: An Overview. *Solid State Ionics* **2009**, *180* (14–16), 911–916. https://doi.org/10.1016/j.ssi.2009.03.022.

(6) Manthiram, A.; Yu, X.; Wang, S. Lithium Battery Chemistries Enabled by Solid-State Electrolytes. *Nat. Rev. Mater.* **2017**, *2* (4), 1–16. https://doi.org/10.1038/natrevmats.2016.103.

(7) Lau, J.; DeBlock, R. H.; Butts, D. M.; Ashby, D. S.; Choi, C. S.; Dunn, B. S. Sulfide Solid Electrolytes for Lithium Battery Applications. *Adv. Energy Mater.* **2018**, *8* (27), 1800933. https://doi.org/10.1002/aenm.201800933.

(8) Croce, F.; Appetecchi, G. B.; Persi, L.; Scrosati, B. (Al_2O_3, TiO_2) Nanocomposite Polymer Electrolytes for Lithium Batteries, F. Croce, B. Scrosati, Nature (1998). *Nat. Lett.* **1998**, *394* (July), 456–458.

(9) Bachman, J. C.; Muy, S.; Grimaud, A.; Chang, H.-H.; Pour, N.; Lux, S. F.; Paschos, O.; Maglia, F.; Lupart, S.; Lamp, P.; et al. Inorganic Solid-State Electrolytes for Lithium Batteries: Mechanisms and Properties Governing Ion Conduction. *Chem. Rev.* **2016**, *116* (1), 140–162. https://doi.org/10.1021/acs.chemrev.5b00563.

(10) Zhang, Z.; Shao, Y.; Lotsch, B.; Hu, Y.-S.; Li, H.; Janek, J.; Nazar, L. F.; Nan, C.-W.; Maier, J.; Armand, M.; et al. New Horizons for Inorganic Solid State Ion Conductors. *Energy Environ. Sci.* **2018**, *11* (8), 1945–1976. https://doi.org/10.1039/C8EE01053F.

(11) Janek, J.; Zeier, W. G. A Solid Future for Battery Development. *Nat. Energy* **2016**, *1* (9), 16141. https://doi.org/10.1038/nenergy.2016.141.

(12) Thompson T., D.; Sharafi, A.; Johannes M. D., D.; Huq A., D.; Allen J. L., D.; Wolfenstine J., D.; Sakamoto, J. A Tale of Two Sites: On Defining the Carrier Concentration in Garnet-Based Ionic Conductors for Advanced Li Batteries. *Adv. Energy Mater.* **2015**, *5* (11).

(13) Buannic, L.; Orayech, B.; López Del Amo, J. M.; Carrasco, J.; Katcho, N. A.; Aguesse, F.; Manalastas, W.; Zhang, W.; Kilner, J.; Llordés, A. Dual Substitution Strategy to Enhance Li^+ Ionic Conductivity in $Li_7La_3Zr_2O_{12}$ Solid Electrolyte. *Chem. Mater.* **2017**, *29* (4), 1769–1778. https://doi.org/10.1021/acs.chemmater.6b05369.

(14) Xu, X.; Wen, Z.; Wu, X.; Yang, X.; Gu, Z. Lithium Ion-Conducting Glass-Ceramics of Li1.5Al0.5Ge1.5(PO4)3-XLi2O (X=0.0-0.20) with Good Electrical and Electrochemical Properties. *J. Am. Ceram. Soc.* **2007**, *90* (9), 2802–2806. https://doi.org/10.1111/j.1551-2916.2007.01827.x.

(15) Kamaya, N.; Homma, K.; Yamakawa, Y.; Hirayama, M.; Kanno, R.; Yonemura, M.; Kamiyama, T.; Kato, Y.; Hama, S.; Kawamoto, K.; et al. A Lithium Superionic Conductor. *Nat. Mater.* **2011**, *10* (9), 682–686. https://doi.org/10.1038/nmat3066.

(16) Cao, C.; Li, Z. Bin; Wang, X. L.; Zhao, X. B.; Han, W. Q. Recent Advances in Inorganic Solid Electrolytes for Lithium Batteries. *Front. Energy Res.* **2014**, *2* (JUN), 1–10. https://doi.org/10.3389/fenrg.2014.00025.

(17) Seino, Y.; Ota, T.; Takada, K.; Hayashi, A.; Tatsumisago, M. A Sulphide Lithium Super Ion Conductor Is Superior to Liquid Ion Conductors for Use in Rechargeable Batteries. *Energy Environ. Sci.* **2014**, *7* (2), 627–631. https://doi.org/10.1039/C3EE41655K.

(18) Deiseroth, H.-J.; Kong, S.-T.; Eckert, H.; Vannahme, J.; Reiner, C.; Zaiß, T.; Schlosser, M. Li\down{6}PS\down{5}X: A Class of Crystalline Li-Rich Solids With an Unusually High Li\p{+} Mobility. *Angew. Chemie Int. Ed.* **2008**, *47* (4), 755–758. https://doi.org/10.1002/anie.200703900.

(19) Stallworth, P. E.; Fontanella, J. J.; Wintersgill, M. C.; Scheidler, C. D.; Immel, J. J.; Greenbaum, S. G.; Gozdz, A. S. NMR, DSC and High Pressure Electrical Conductivity Studies of Liquid and Hybrid Electrolytes. *J. Power Sources* **1999**, *81–82*, 739–747. https://doi.org/10.1016/S0378-7753(99)00144-5.

(20) Kim, K.; Siegel, D. J. Correlating Lattice Distortions, Ion Migration Barriers, and Stability in Solid Electrolytes. *J. Mater. Chem. A* **2019**, *7* (7), 3216–3227. https://doi.org/10.1039/C8TA10989C.

(21) de Klerk, N. J. J.; Ros{\l}o\'{n}, I.; Wagemaker, M. Diffusion Mechanism of Li Argyrodite Solid Electrolytes for Li-Ion Batteries and Prediction of Optimized Halogen Doping: The Effect of Li Vacancies, Halogens, and Halogen Disorder. *Chem. Mater.* **2016**, *28* (21), 7955–7963. https://doi.org/10.1021/acs.chemmater.6b03630.

(22) Kraft, M. A.; Culver, S. P.; Calderon, M.; Böcher, F.; Krauskopf, T.; Senyshyn, A.; Dietrich, C.; Zevalkink, A.; Janek, J.; Zeier, W. G. Influence of Lattice Polarizability on the Ionic Conductivity in the Lithium Superionic Argyrodites Li\down{6}PS\down{5}X (X = Cl, Br, I). *J. Am. Chem. Soc.* **2017**, *139* (31), 10909–10918. https://doi.org/10.1021/jacs.7b06327.

(23) Rayavarapu, P. R.; Sharma, N.; Peterson, V. K.; Adams, S. Variation in Structure and Li\p{+}-Ion Migration in Argyrodite-Type Li\down{6}PS\down{5}X (X = Cl, Br, I) Solid Electrolytes. *J. Solid State Electrochem.* **2012**, *16* (5), 1807–1813. https://doi.org/10.1007/s10008-011-1572-8.

(24) Rao, R. P.; Adams, S. Studies of Lithium Argyrodite Solid Electrolytes for All-Solid-State Batteries. *Phys. status solidi* **2011**, *208* (8), 1804–1807. https://doi.org/10.1002/pssa.201001117.

(25) Chen, H. M.; Maohua, C.; Adams, S. Stability and Ionic Mobility in Argyrodite-Related Lithium-Ion Solid Electrolytes. *Phys. Chem. Chem. Phys.* **2015**, *17* (25), 16494–16506. https://doi.org/10.1039/C5CP01841B.

(26) Pecher, O.; Kong, S.-T.; Goebel, T.; Nickel, V.; Weichert, K.; Reiner, C.; Deiseroth, H.-J.; Maier, J.; Haarmann, F.; Zahn, D. Atomistic Characterisation of Li\p{+} Mobility and Conductivity in Li\down{7−x}PS\down{6−x}I\down{x} Argyrodites from Molecular Dynamics Simulations, Solid-State NMR, and Impedance Spectroscopy. *Chem. - A Eur. J.* **2010**, *16* (28), 8347–8354. https://doi.org/10.1002/chem.201000501.

(27) Yu, C.; Ganapathy, S.; de Klerk, N. J. J.; Ros{\l}o\'{n}, I.; van Eck, E. R. H.; Kentgens, A. P. M.; Wagemaker, M. Unravelling Li-Ion Transport from Picoseconds to Seconds: Bulk versus Interfaces in an Argyrodite Li\down{6}PS\down{5}Cl-Li\down{2}S All-Solid-State Li-Ion Battery. *J. Am. Chem. Soc.* **2016**, *138* (35), 11192–11201. https://doi.org/10.1021/jacs.6b05066.

(28) Hoelzel, M.; Senyshyn, A.; Juenke, N.; Boysen, H.; Schmahl, W.; Fuess, H. High-Resolution Neutron Powder Diffractometer SPODI at Research Reactor FRM II. *Nucl. Instruments Methods Phys. Res. Sect. A* **2012**, *667*, 32–37. https://doi.org/10.1016/j.nima.2011.11.070.

(29) Rodr\'{i}guez-Carvajal, J. Recent Developments of the Program FULLPROF, in Commission on Powder Diffraction (IUCr). *Newsletter* **2011**, *26*, 12–19.

(30) Filik, J.; Ashton, A. W.; Chang, P. C. Y.; Chater, P. A.; Day, S. J.; Drakopoulos, M.; Gerring, M. W.; Hart, M. L.; Magdysyuk, O. V.; Michalik, S.; et al. Processing Two-Dimensional X-Ray Diffraction and Small-Angle Scattering Data in DAWN 2. *J. Appl. Crystallogr.* **2017**, *50* (3), 959–966. https://doi.org/10.1107/S1600576717004708.

(31) Kong, S. T.; Gün, Ö.; Koch, B.; Deiseroth, H. J.; Eckert, H.; Reiner, C. Structural Characterisation of the Li Argyrodites Li\down{7}PS\down{6} and Li\down{7}PSe\down{6} and Their Solid Solutions: Quantification of Site Preferences by MAS-NMR Spectroscopy. *Chem. - A Eur. J.* **2010**, *16* (17), 5138–5147. https://doi.org/10.1002/chem.200903023.

(32) Adams, S. Relationship between Bond Valence and Bond Softness of Alkali Halides and Chalcogenides. *Acta Crystallogr. Sect. B Struct. Sci.* **2001**, *57* (3), 278–287. https://doi.org/10.1107/S0108768101003068.

(33) Buschmann, H.; Dölle, J.; Berendts, S.; Kuhn, A.; Bottke, P.; Wilkening, M.; Heitjans, P.; Senyshyn, A.; Ehrenberg, H.; Lotnyk, A.; et al. Structure and Dynamics of the Fast Lithium Ion Conductor "Li\down{7}La\down{3}Zr\down{2}O\down{12}." *Phys. Chem. Chem. Phys.* **2011**, *13* (43), 19378. https://doi.org/10.1039/c1cp22108f.

(34) Momma, K.; Izumi, F. VESTA 3 for Three-Dimensional Visualization of Crystal, Volumetric and Morphology Data. *J. Appl. Crystallogr.* **2011**, *44* (6), 1272–1276. https://doi.org/10.1107/S0021889811038970.

(35) Momma, K.; Ikeda, T.; Belik, A. A.; Izumi, F. Dysnomia, a Computer Program for Maximum-Entropy Method (MEM) Analysis and Its Performance in the MEM-Based Pattern Fitting. *Powder Diffr.* **2013**, *28* (3), 184–193. https://doi.org/10.1017/S088571561300002X.

(36) Weber, D. A.; Senyshyn, A.; Weldert, K. S.; Wenzel, S.; Zhang, W.; Kaiser, R.; Berendts, S.; Janek, J.; Zeier, W. G. Structural Insights and 3D Diffusion Pathways within the Lithium Superionic Conductor Li10GeP2S12. *Chem. Mater.* **2016**, *28* (16), 5905–5915. https://doi.org/10.1021/acs.chemmater.6b02424.

(37) Stöffler, H.; Zinkevich, T.; Yavuz, M.; Senyshyn, A.; Kulisch, J.; Hartmann, P.; Adermann, T.; Randau, S.; Richter, F. H.; Janek, J.; et al. Li\p{+}-Ion Dynamics in $\upbeta$-Li\down{3}PS\down{4} Observed by NMR: Local Hopping and Long-Range Transport. *J. Phys. Chem. C* **2018**, *122* (28), 15954–15965. https://doi.org/10.1021/acs.jpcc.8b05431.

(38) Senyshyn, A.; Boysen, H.; Niewa, R.; Banys, J.; Kinka, M.; Burak, Y.; Adamiv, V.; Izumi, F.; Chumak, I.; Fuess, H. High-Temperature Properties of Lithium Tetraborate $Li_2B_4O_7$. *J. Phys. D. Appl. Phys.* **2012**, *45* (17). https://doi.org/10.1088/0022-3727/45/17/175305.

(39) Robinson, K.; Gibbs, G. V.; Ribbe, P. H. Quadratic Elongation: A Quantitative Measure of Distortion in Coordination Polyhedra. *Science (80-.).* **1971**, *172* (3983), 567–570. https://doi.org/10.1126/science.172.3983.567.

(40) Hanghofer, I.; Brinek, M.; Eisbacher, S. L.; Bitschnau, B.; Volck, M.; Hennige, V.; Hanzu, I.; Rettenwander, D.; Wilkening, H. M. R. Substitutional Disorder: Structure and Ion Dynamics of the Argyrodites Li\down{6}PS\down{5}Cl, Li\down{6}PS\down{5}Br and Li\down{6}PS\down{5}I. *Phys. Chem. Chem. Phys.* **2019**, *21* (16), 8489–8507. https://doi.org/10.1039/C9CP00664H.

(41) Kraft, M. A.; Ohno, S.; Zinkevich, T.; Koerver, R.; Culver, S. P.; Fuchs, T.; Senyshyn, A.; Indris, S.; Morgan, B. J.; Zeier, W. G. Inducing High Ionic Conductivity in the Lithium Superionic Argyrodites $Li_{6+x}P_{1-x}Ge_xS_5I$ for All-Solid-State Batteries. *J. Am. Chem. Soc.* **2018**, *140* (47), 16330–16339. https://doi.org/10.1021/jacs.8b10282.

(42) Stöffler, H.; Zinkevich, T.; Yavuz, M.; Hansen, A.-L.; Knapp, M.; Bednarčík, J.; Randau, S.; Richter, F. H.; Janek, J.; Ehrenberg, H.; et al. Amorphous versus Crystalline Li\down{3}PS\down{4}: Local Structural Changes during Synthesis and Li Ion Mobility. *J. Phys. Chem. C* **2019**, *123* (16), 10280–10290. https://doi.org/10.1021/acs.jpcc.9b01425.

(43) Eckert, H.; Zhang, Z.; Kennedy, J. H. Structural Transformation of Non-Oxide Chalcogenide Glasses. The Short-Range Order of Lithium Sulfide (Li\down{2}S)-Phosphorus Pentasulfide (P\down{2}S\down{5}) Glasses Studied by Quantitative \p{31}P and \p{6,7}Li High-

Resolution Solid-State NMR. *Chem. Mater.* **1990**, *2* (3), 273–279. https://doi.org/10.1021/cm00009a017.

(44) Kaus, M.; Stöffler, H.; Yavuz, M.; Zinkevich, T.; Knapp, M.; Ehrenberg, H.; Indris, S. Local Structures and Li Ion Dynamics in a Li\down{10}SnP\down{2}S\down{12}-Based Composite Observed by Multinuclear Solid-State NMR Spectroscopy. *J. Phys. Chem. C* **2017**, *121* (42), 23370–23376. https://doi.org/10.1021/acs.jpcc.7b08350.

(45) Dietrich, C.; Weber, D. A.; Sedlmaier, S. J.; Indris, S.; Culver, S. P.; Walter, D.; Janek, J.; Zeier, W. G. Lithium Ion Conductivity in Li\down{2}S-P\down{2}S\down{5} Glasses - Building Units and Local Structure Evolution during the Crystallization of Superionic Conductors Li\down{3}PS\down{4}, Li\down{7}P\down{3}S\down{11} and Li\down{4}P\down{2}S\down{7}. *J. Mater. Chem. A* **2017**, *5* (34), 18111–18119. https://doi.org/10.1039/C7TA06067J.

(46) Sedlmaier, S. J.; Indris, S.; Dietrich, C.; Yavuz, M.; Dräger, C.; von Seggern, F.; Sommer, H.; Janek, J. Li\down{4}PS\down{4}I: A Li\p{+} Superionic Conductor Synthesized by a Solvent-Based Soft Chemistry Approach. *Chem. Mater.* **2017**, *29* (4), 1830–1835. https://doi.org/10.1021/acs.chemmater.7b00013.

(47) Yu, C.; Ganapathy, S.; van Eck, E. R. H.; van Eijck, L.; Basak, S.; Liu, Y.; Zhang, L.; Zandbergen, H. W.; Wagemaker, M. Revealing the Relation between the Structure, Li-Ion Conductivity and Solid-State Battery Performance of the Argyrodite Li\down{6}PS\down{5}Br Solid Electrolyte. *J. Mater. Chem. A* **2017**, *5* (40), 21178–21188. https://doi.org/10.1039/C7TA05031C.

(48) Bloembergen, N.; Purcell, E. M.; Pound, R. V. Relaxation Effects in Nuclear Magnetic Resonance Absorption. *Phys. Rev.* **1948**, *73* (7), 679–712. https://doi.org/10.1103/PhysRev.73.679.

(49) Knauth, P.; Schoonman, J. *Nanocomposites. Ionic Conducting Materials and Structural Spectroscopies*; Knauth, P., Schoonman, J., Eds.; Springer Science+Business Media, LLC: New York, 2008.

(50) Einstein, A. Über Die von Der Molekularkinetischen Theorie Der Wärme Geforderte Bewegung von in Ruhenden Flüssigkeiten Suspendierten Teilchen. *Ann. Phys.* **1905**, *322* (8), 549–560.

(51) Smoluchowski, M. von. Zur Kinetischen Theorie Der Brownschen Molekularbewegung Und Der Suspensionen. *Ann. Phys.* **1906**, *326* (14), 756–780.

(52) Mehrer, H. *Diffusion in Solids Fundamentals, Methods, Materials, Diffusion-Controlled Process*; Fulde, P., Klitzing, K. von, Eds.; Springe-Verlag Berlin Heidelberg, 2009.

(53) McKee, R. A. A Generalization of the Nernst-Einstein Equation for Self-Diffusion in High Defect Concentration Solids. *Solid State Ionics* **1981**, *5*, 133–136. https://doi.org/10.1016/0167-2738(81)90210-1.

(54) Stejskal, E. O.; Tanner, J. E. Spin Diffusion Measurements: Spin Echoes in the Presence of a Time-Dependent Field Gradient. *J. Chem. Phys.* **1965**, *42* (1), 288–292. https://doi.org/10.1063/1.1695690.

(55) Bunde, A.; Maass, P.; Meyer, M. *Diffusion in Condensed Matter*; Kärger, J., Heitjans, P., Haberland, R., Eds.; Berlin: Springer, 1998.

(56) Boulineau, S.; Courty, M.; Tarascon, J.-M.; Viallet, V. Mechanochemical Synthesis of Li-Argyrodite Li\down{6}PS\down{5}X (X=Cl, Br, I) as Sulfur-Based Solid Electrolytes for All Solid State Batteries Application. *Solid State Ionics* **2012**, *221*, 1–5. https://doi.org/10.1016/j.ssi.2012.06.008.

(57) Wenzel, S.; Sedlmaier, S. J.; Dietrich, C.; Zeier, W. G.; Janek, J. Interfacial Reactivity and Interphase Growth of Argyrodite Solid Electrolytes at Lithium Metal Electrodes. *Solid State Ionics* **2018**, *318*, 102–112. https://doi.org/10.1016/j.ssi.2017.07.005.

(58) Deiseroth, H.-J.; Maier, J.; Weichert, K.; Nickel, V.; Kong, S.-T.; Reiner, C. Li\down{7}PS\down{6} and Li\down{6}PS\down{5}X (X: Cl, Br, I): Possible Three-Dimensional Diffusion Pathways for Lithium Ions and Temperature Dependence of the Ionic Conductivity by Impedance Measurements. *Zeitschrift für Anorg. und Allg. Chemie* **2011**, *637* (10), 1287–1294. https://doi.org/10.1002/zaac.201100158.

(59) Adeli, P.; Bazak, J. D.; Park, K. H.; Kochetkov, I.; Huq, A.; Goward, G. R.; Nazar, L. F. Boosting Solid-State Diffusivity and Conductivity in Lithium

Superionic Argyrodites by Halide Substitution. *Angew. Chemie Int. Ed.* **2019**, *58* (26), 8681–8686. https://doi.org/10.1002/anie.201814222.

(60) Zhou, L.; Park, K.-H.; Sun, X.; Lalère, F.; Adermann, T.; Hartmann, P.; Nazar, L. F. Solvent-Engineered Design of Argyrodite Li\down{6}PS\down{5}X (X = Cl, Br, I) Solid Electrolytes with High Ionic Conductivity. *ACS Energy Lett.* **2019**, *4* (1), 265–270. https://doi.org/10.1021/acsenergylett.8b01997.

Table of contents (TOC) graphic